

Zonal momentum budget of the Madden-Julian Oscillation: role of the time-mean flow

Jialin Lin¹, Minghua Zhang² and Brian Mapes¹

¹ **NOAA-CIRES Climate Diagnostics Center, Boulder, CO 80305**

² **State University of New York, Stony Brook, NY 11794**

July, 2003

ABSTRACT

In theoretical models of the Madden-Julian Oscillation (MJO), time-mean flow was often neglected, and the resultant zonal momentum balance at the equator is between local tendency and pressure gradient force. In the observed MJO, however, the dominant balance at the equator is between advective tendency and pressure gradient force. The local tendency is small, as well as the convective momentum flux convergence suggested by budget residual. The advective tendency is dominated by the linear terms associated with time-mean zonal and vertical flows. Simple scale analysis shows that over the warm pool region, the time-mean upper-level easterly wind, zonal divergence, and upward motion are bound to cause an advective tendency much larger than the local tendency at the MJO time-scale. Therefore, the linear advection terms associated with time-mean flow need to be included in theoretical models of the MJO.

1. Introduction

Discovered by Madden and Julian (1971, 1972), the Madden-Julian Oscillation (MJO) is the dominant intraseasonal mode of variability in tropical convection and circulation (e.g. Weickmann et al. 1985, Lau and Chan 1985, Salby and Hendon 1994, Wheeler and Kiladis 1999). It affects a wide range of tropical weather such as the onset and breaks of the Indian and Australian summer monsoons (e.g. Yasunari 1979, Hendon and Liebmann 1990), and the formation of tropical cyclones (e.g. Nakazawa 1986, Liebmann et al. 1994). It also drives teleconnections to the extratropics (e.g., Lau and Phillips 1986, Winkler et al. 2001) and impacts some important extratropical weather (e.g. Higgins and Mo 1997, Higgins et al. 2000). On a longer timescale, the MJO is observed to trigger or terminate some El Nino events (e.g. Kessler et al. 1995, Takayabu et al. 1999, Bergman et al. 2001). Therefore, the MJO is important for both extended-range weather forecasting and long-term climate prediction.

Tropical intraseasonal variability is poorly simulated in general circulation models (GCMs). Typically, simulated phenomena are too weak and propagate too fast (e.g. Hayashi and Sumi 1986, Hayashi and Golder 1986, 1988, 1993, Lau et al. 1988, Slingo et al. 1996). It is our hope that observational studies of major budget terms may offer useful guidance on how to improve MJO simulations and forecasts in models.

When comparing intraseasonal oscillations in 15 GCMs as part of the Atmospheric Model Intercomparison Project (AMIP), Slingo et al. (1996) found that GCMs which produce more realistic intraseasonal variability also tend to produce a stronger seasonal cycle of basic flow, suggesting that an accurate description of the time-mean

flow may be a prerequisite for producing a realistic intraseasonal oscillation, but the reason for this correlation was not clear.

In theoretical models of the MJO, the time-mean flow was often neglected. In the classic equatorial wave model developed by Matsuno (1966) and Lindzen (1967), the momentum equation was linearized about a state at rest, neglecting the linear advection terms associated with time-mean flow, the nonlinear advection terms, and the eddy momentum flux convergence. The resultant zonal momentum balance at the equator is simply between the local tendency and the pressure gradient force:

$$\frac{\partial u'}{\partial t} = -\frac{\partial \phi'}{\partial x} \quad (1)$$

Among the different wave modes predicted by the model, the Kelvin wave is most similar to the observed MJO because the MJO (1) propagates eastward and (2) has a negligible meridional wind anomaly near the equator. Therefore, a Kelvin-wave model coupled with diabatic heating, which is schematically shown in Fig. 1, was often used to study wave-heating feedback mechanisms in the MJO, such as the wave-CISK (Convective Instability of the Second Kind) mechanism (Lau and Peng 1987, Chang and Lim 1988, Crum and Dunkerton 1992, Cho et al. 1994), the frictional wave-CISK mechanism (Wang 1988), the WISHE (Wave Induced Surface Heat Exchange) mechanism (Emanuel 1987, Neelin et al. 1987), and the cloud-radiation feedback mechanism (Mehta and Smith 1997). Time-mean zonal wind is included in the WISHE models, but its value is generally small (representing time-mean surface wind in the warm pool region) and the dominant zonal momentum

balance is still Eq. 1.

However, two other characteristics of the observed MJO raised the question whether it is really a Kelvin wave, or a completely different identity. The first characteristic is the dispersion relation. Wheeler and Kiladis (1999) presented a plot of the variance of near-equatorial outgoing longwave radiation (OLR) as a function of frequency and zonal wavenumber. After removing a red-noise background, these plots showed all of the equatorial wave modes predicted by Matsuno (1966) and Lindzen (1967). However, the MJO appeared as a distinct mode separated from the Kelvin mode, with a fixed frequency independent of wavenumber. This contrasts with the dispersion relation of the Kelvin wave in which frequency is proportional to wavenumber. The second characteristic is the phase difference between zonal wind u and geopotential height Z . In a neutral Kelvin wave (Fig. 1), the balance between local tendency and pressure gradient force (Eq. 1) leads to an in-phase relationship between u and Z . In the observed MJO, however, quarter-cycle phase difference between u and Z was found in both the lower troposphere (Madden and Julian 1972) and the upper troposphere (Kiladis and Weickmann 1992, Hsu 1996). Because both the dispersion relation and the u - Z phase relationship in the Kelvin wave are consequences of its zonal momentum equation Eq. 1, the different characteristics in the observed MJO suggest that some terms other than the local tendency or pressure gradient force may contribute to the MJO zonal momentum budget.

Therefore, the above studies raise the following questions for observation: What are the dominant terms in the MJO zonal momentum budget? Does the terms ne-

glected in Eq. 1 (the advection terms and eddy momentum flux convergence) play an important role in the MJO?

Momentum budget was calculated in previous studies for the mesoscale convective systems (Gallus and Johnson 1992, Wu and Yanai 1994, Zhang and Lin 1997, Mapes and Wu 2001), the easterly waves (Stevens 1979), and the seasonal mean of tropical atmosphere (Carr and Bretherton 2001, Lin and Mapes 2003). However, no calculation was done for the MJO. In this study, we calculated the MJO zonal momentum budget using NCEP and ECMWF reanalysis data. The main budget uncertainties associated with pressure gradient forces and advection terms are reduced by (1) comparing between NCEP and ECMWF reanalyses, whose consistencies gave us more confidence, and (2) constructing long-term (15 years) MJO composite and considering only the statistically significant signals, which are likely real signals unless there are errors in the reanalyses which are systematically coherent with the MJO.

A surprising finding is that the dominant balance in the MJO zonal momentum budget at the equator is between the advective tendency and the pressure gradient force, which is fundamentally different from the Kelvin wave. The local tendency is small, as well as the convective momentum flux convergence suggested by budget residual. The advective tendency is dominated by the linear terms associated with time-mean zonal and vertical motions. Simple scale analysis shows that over the warm pool region, the time-mean upper-level upward motion, zonal divergence, and easterly wind are bound to cause an advective tendency much larger than the local tendency at the MJO time-scale. Therefore, the observed MJO is dynamically different from

the Kelvin wave, and the linear advection terms associated with time-mean flow need to be included when modeling the MJO wave structure.

The datasets used in this study are described in section 2. The time filtering and intraseasonal composite (regression) methods are described in section 3. The zonal momentum budget results are reported in section 4. Conclusions and discussions are given in section 5.

2. Data

The datasets used include 15 years (1979-1999) of daily reanalyses data from two different centers: NCEP and ECMWF. The variables used include upper air wind, geopotential height, and vertical pressure velocity. The horizontal resolution is 2.5 degree longitude by 2.5 degree latitude. Zonal momentum budget is calculated for both reanalyses following Carr and Bretherton (2001). The zonal momentum equation can be written:

$$\frac{\partial u}{\partial t} = -u \frac{\partial u}{\partial x} - v \frac{\partial u}{\partial y} - \omega \frac{\partial u}{\partial p} + f(y)v - \frac{\partial \phi}{\partial x} + X \quad (2)$$

where u is the zonal wind, v the meridional wind, ω the vertical pressure velocity; x and y are E-W and N-S distance, f the Coriolis parameter, and ϕ the geopotential. Here X represents accelerations due to all subgrid-scale processes. In the free troposphere (above the effects of boundary layer turbulence eddies), over the open ocean (away from the effects of topographically induced gravity waves), it is reasonable to assume that convective momentum transport is the dominant subgrid-scale process.

Under this assumption, we can write:

$$X = \frac{\partial}{\partial p} < u' \omega' > \quad (3)$$

where $< \quad >$ denotes an ensemble average at a given pressure level, and primes denote the local perturbation from the ensemble average. In this way, we define X to be the acceleration of the zonal flow due to convergence of zonal momentum flux. The zonal momentum flux at each level is then obtained by integrating upward from the surface:

$$< u' \omega' > (p) = < u' \omega' >_{sfc} - \int_p^{p_{sfc}} X(p) dp \quad (4)$$

Each budget term of Eq. 2 was calculated using daily data at each 2.5 degree longitude by 2.5 degree latitude grid. Derivatives were evaluated using central difference scheme. The results were then averaged to pentad data along the equator (between 5N and 5S) with a zonal resolution of 10 degree longitude.

For constructing the MJO composite, we also used 15 years (1979-1993) of pentad CMAP precipitation data (Xie and Arkin 1997). The horizontal resolution is also 2.5 degree longitude by 2.5 degree latitude. We averaged the data along the equator (between 5N and 5S) with a zonal resolution of 5 degree longitude.

3. Method

The MJO is a broad-band phenomenon, with an averaged period of 45 days but a fairly wide spread from 20 to 80 days (see review by Madden and Julian 1994). Its deep convection signal is dominated by wavenumber 1-6, while its circulation signal is dominated by wavenumber 1 (e.g. Salby and Hendon 1994, Wheeler and Kiladis

1999). The variance of its deep convection signal has two centers: western Pacific and eastern Indian Ocean, and over these two centers, the MJO propagates eastward with a slow phase speed of about 5 m/s (e.g. Wheeler and Kiladis 1999, Lin et al. 2003).

These characteristics were used to isolate the MJO signal. Lin et al. (2003) discussed the different methods used in previous observational and modeling studies. The different methods often give qualitatively similar results in terms of propagation characteristics and phase difference among different variables. This consistency is apparently because strong intraseasonally filtered deep convection fluctuations along the equator are dominated, both in number and strength, by coherent eastward propagating events (Wang and Rui 1990). Linear composite methods used in most of the previous studies (e.g. phase sum, correlation, regression) are apparently dominated by these strong eastward propagating events. The method used in this study is a similar to that used in Lin et al. (2003). The procedure is as follows:

- (1) The zonal means were first removed from all datasets.
- (2) The datasets were then filtered using a 30-70 day Murakami (1976) filter, whose response function is shown in Fig. 2. The central frequency corresponds to a period of 45 day. The half amplitude is at periods of 30 day and 70 day. We also tested the Lanczos filter (Duchan 1979), and the results were not sensitive.
- (3) For the master MJO index, we filtered the CMAP precipitation in time as above, and also in space, retaining wavenumbers 1-6.
- (4) To study the MJO phenomena in its two centers of variance, we averaged the

datasets in two boxes: a western Pacific box between 150-160E and 5N-5S, and an eastern Indian Ocean box between 80-90E and 5N-5S. For each box, an MJO composite was constructed using linear regression with respect to the filtered CMAP precipitation at the same box, and the regression coefficient was multiplied by one standard deviation of the filtered CMAP precipitation. The confidence level of linear correlation was estimated following Oort and Yienger (1996).

(5) Regressions were done for all seasons of the year, as well as for individual seasons (December-February, March-May, June-August, and September-November).

4. Results

a. Vertical structure of the MJO at the equator

Before examining the MJO zonal momentum budget, we first look at the vertical structure of the MJO, which is important for understanding later the zonal momentum budget. The composite vertical structure of MJO in the western Pacific is shown in Fig. 3 using 15 years (1979-1993) of NCEP reanalysis data averaged between 5N-5S and 150-160E. The time lag is with respect to the time of maximum precipitation. The time evolution is from the right to the left, showing the local evolution of measured variables as the eastward-moving MJO passes the measurement longitude. The zonal wind u (Fig. 3a) shows a simple two-layer structure with the upper layer out of phase with the lower layer. This two-layer structure is well-known from many previous observations (e.g. Madden and Julian 1971, 1972, Weickmann et al. 1985, Knutson and Weickmann 1987). However, an interesting feature which did not bring much

attention is that the maxima of both the two layers are at a very high altitude, not the 850 mb and 200 mb levels used in many previous MJO studies. The maximum of the lower layer is around 600 mb (just below the 0 C level), while that of the upper layer is around 150 mb (just below the tropopause). It means that at the time of maximum precipitation, the zonal inflow is just below the 0 C level, and the zonal outflow is just below the tropopause. Consistent with this inflow-outflow feature, the vertical motion (Fig. 3b) concentrates in the upper troposphere. For clarity, the two-dimensional flow is plotted using arrows in Fig. 3c. This middle troposphere inflow and near tropopause outflow structure are consistent with the top-heavy heating profile in the MJO shown in Lin et al. (2003). Therefore, the MJO is associated with a vertical mode concentrating in the upper half of the troposphere.

The vertical motion shows a westward phase tilt with height. It develops first in the lower troposphere, and then shifts upward as it intensifies. This westward phase tilt of vertical motion is consistent with the westward phase tilt of the associated heating anomaly shown in Lin et al. (2003), which is caused by vertical phase tilts of convective heating in the earlier stages, and stratiform heating in the later stages.

The geopotential height Z (contours in Fig. 3c) has a large amplitude in the near-tropopause outflow layer but a small amplitude in the middle-troposphere inflow layer. Z lags u at both the inflow and outflow layers. The phase differences is about 5 days in the outflow layer and 10 days in the inflow layer. The phase difference in the upper layer is smaller than those found by Kiladis and Weickmann (1992) and Hsu (1996). The reason is that we removed the zonal mean component from all datasets while

they didn't, and our test using data retaining zonal mean showed that the zonal mean component in geopotential height increases the u and Z phase difference in western Pacific (not shown).

The MJO has two centers of variance: the western Pacific and the eastern Indian Ocean. The vertical structure over the eastern Indian Ocean is shown in Fig. 4 using NCEP reanalysis data averaged between 5N-5S and 80-90E. The wave structure is quite similar to that over the western Pacific (Fig. 3), with similar middle-troposphere inflow and near-tropopause outflow, and similar u - Z phase difference. This u - Z phase difference over the eastern Indian Ocean was not found in Kiladis and Weickmann (1992) and Hsu (1996), which is because the zonal mean component of geopotential height retained in their data decreases the u and Z phase difference in that region (not shown).

Composites constructed using 15 years (1979-1993) of ECMWF reanalysis data over the western Pacific and the eastern Indian Ocean show similar wave structure as the NCEP data (not shown). We also checked the composites for each individual seasons (DJF, MAM, JJA and SON) at both western Pacific and eastern Indian Ocean. The wave structures are generally similar to the all-seasons composites except for boreal summer (JJA) over the eastern Indian Ocean (not shown). Many previous studies have shown that the boreal summer intraseasonal oscillation is characterized by prominent northward propagation and a 35-day period (e.g. Yasunari 1979, Hartmann et al. 1992), which is quite different from the eastward-propagating 45-day MJO mode originally described by Madden and Julian (1971, 1972), although there

are some connections between the eastward propagating mode and the northward propagating mode (see review by Madden and Julian 1994). Therefore we will restrict our study to the eastward-propagating MJO and will report the results for the northward-propagating boreal summer intraseasonal oscillation in a separate study.

In summary, the equatorial wave structure of the MJO has the following three characteristics:

- (1) It is associated with a vertical mode concentrated in the upper half of the troposphere, with middle-troposphere inflow and near-tropopause outflow at the time of maximum precipitation.
- (2) The vertical motion has a westward phase tilt with height.
- (3) Geopotential height lags zonal wind by about 5-10 days at both the inflow and outflow layers.

As discussed in the introduction, the u - Z phase difference suggests that some terms other than local tendency or pressure gradient force may contribute to the MJO zonal momentum budget. In order to know exactly what these “extra” terms are, in the next section we directly examine the zonal momentum budget.

b. Zonal momentum budget of the MJO

From Eq. 2, we can write the MJO anomalous zonal momentum equation:

$$\frac{\partial \tilde{u}'}{\partial t} = -\frac{\partial \tilde{\phi}'}{\partial x} + \tilde{f}v' + (-u\frac{\partial \tilde{u}'}{\partial x} - v\frac{\partial \tilde{u}'}{\partial y} - \omega\frac{\partial \tilde{u}'}{\partial p}) + \tilde{X}' \quad (5)$$

where tilde denotes deviation from zonal mean, prime denotes 30-70 day temporally

filtered anomaly. The MJO zonal momentum budget terms at the equator (averaged between 150E-160E and 5N-5S) are shown in Figs. 5 and 6 for NCEP and ECMWF reanalyses, respectively. The Coriolis force is small near the equator and is not shown. The two different reanalyses show similar patterns for each of the three budget terms, giving us more confidence on the results. Moreover, only signals with correlation above the 95% confidence level are plotted in Figs. 5 and 6. These signals are likely real unless there are errors in the reanalyses which are systematically coherent with the MJO. A surprising result from Figs. 5 and 6 is that in the upper troposphere, the dominant balance is between the advection terms and the pressure gradient force, and the local tendency is very small. This is fundamentally different from the dominant balance in the Kelvin wave, which is between the local tendency and the pressure gradient force (Eq. 1). The MJO zonal momentum budgets for each individual seasons are similar to the all-season results, with the dominant balance being between advective tendency and pressure gradient force (not shown).

The budget residual is very small for both reanalyses (Fig. 7), suggesting that convective momentum transport is not important for the MJO zonal momentum budget. This is consistent with the GCM modeling results of Inness and Gregory (1997) that including convective momentum transport does not improve the intraseasonal variability. Both reanalyses show similar patterns for the small budget residual, as well as the implied eddy momentum flux (Fig. 8), giving us more confidence on the budget results. The eddy momentum flux above 700 mb is nearly in phase with precipitation, suggesting a downgradient transport because zonal wind decrease with

height in the warm pool region (cf. Fig. 12). In the early stages, the momentum flux has a westward phase tilt with height, which is consistent with similar westward phase tilt in vertical motion (Figs. 3b, 4b) and in convective heating shown in Lin et al. (2003).

The large contribution of advective tendency to the MJO zonal momentum budget is intriguing and next we examine what cause this strong advection. The zonal, meridional and vertical components of the advective tendency are shown in Figs. 9a, b and c, respectively. The large advection tendency in the upper troposphere is mainly contributed by zonal advection (Fig. 9a) and vertical advection (Fig. 9c), while that in the lower troposphere is mainly contributed by meridional advection (Fig. 9b). In the following we focus on the zonal and vertical advections in the upper troposphere. Each of these components contain both linear and nonlinear effects, which can be decomposed into (see Appendix):

$$-\overline{u} \frac{\partial \tilde{u}'}{\partial x} = -[\tilde{u}] \frac{\partial \tilde{u}'}{\partial x} - \tilde{u}' \frac{\partial [\tilde{u}]}{\partial x} + \text{other terms} \quad (6)$$

$$-\overline{\omega} \frac{\partial \tilde{u}'}{\partial p} = -[\tilde{\omega}] \frac{\partial \tilde{u}'}{\partial p} - \tilde{\omega}' \frac{\partial [\tilde{u}]}{\partial p} + \text{other terms} \quad (7)$$

where $[\]$ denotes time-mean. On the righthand side of each equation, the first two terms are linear advection terms associated with time-mean zonal asymmetric flow, while the other terms include the linear terms associated with zonal-mean and the nonlinear terms (see Appendix). The first two linear terms were calculated from the corresponding time-mean (15-year mean) and the MJO anomalies, and the other terms were derived as the residual. The results are shown in Fig. 10 and Fig. 11, for

zonal advection and vertical advection, respectively. The zonal advection (Fig. 10) is dominated by the first two linear terms, both of which contribute substantially to the budget. The vertical advection (Fig. 11) is also dominated by the first two linear terms, especially $-\tilde{\omega} \frac{\partial \tilde{u}'}{\partial p}$ (Fig. 11a). Therefore, the zonal momentum budget of the MJO is basically linear.

In summary, the dominant balance of the MJO zonal momentum budget at the equator is between advective tendency and pressure gradient force. The local tendency is small, as well as the eddy momentum flux convergence inferred from budget residual. The advective tendency is dominated by the linear terms associated with time-mean zonal and vertical motions, including $-\tilde{u} \frac{\partial \tilde{u}'}{\partial x}$, $-\tilde{u}' \frac{\partial \tilde{u}}{\partial x}$, and $-\tilde{\omega} \frac{\partial \tilde{u}'}{\partial p}$. Therefore, the MJO zonal momentum budget equation Eq. 5 can be simplified to:

$$\frac{\partial \tilde{u}'}{\partial t} = -\frac{\partial \tilde{\phi}'}{\partial x} - [\tilde{u}] \frac{\partial \tilde{u}'}{\partial x} - \tilde{u}' \frac{\partial [\tilde{u}]}{\partial x} - [\tilde{\omega}] \frac{\partial \tilde{u}'}{\partial p} \quad (8)$$

c. Understanding the linear advection terms

The dominant linear advection terms own their existence to the time-mean zonal wind $[\tilde{u}]$, zonal divergence $\frac{\partial [\tilde{u}]}{\partial x}$, and vertical velocity $[\tilde{\omega}]$. To help understanding these terms, we plot the 15 year (1979-1993) climatological mean of vertical velocity, zonal divergence, and zonal wind in Fig. 12. For consistency with the MJO anomaly, we plot here the zonal asymmetric components, but the zonal means are actually much smaller. The warm pool region has the strongest climatological deep convection in

the world. The deep convection is associated with strong upward motion (Fig. 12a). The vertical velocity profile is very top-heavy, and is therefore associated with strong upper-level zonal divergence concentrating in a thin layer near the tropopause (Fig. 12b). The upper-level zonal wind over the warm pool is easterly (Fig. 12c), which is presumably associated with the Gill (1980) pattern associated with a stationary heating source. The wind is strong within a thin layer near the tropopause because the zonal divergence is concentrated in this layer. Fig. 12 only shows the annual mean, so the upper-level upward motion and zonal divergence are weaker over the eastern Indian Ocean. Long-term composite seasonal variation of upper-level vertical velocity, zonal divergence, and zonal wind (Fig. 13) show that they are actually very strong over the eastern Indian Ocean during northern summer.

When the MJO travels in such a large-scale environment, $-[\tilde{u}]\frac{\partial\tilde{u}'}{\partial x}$ (Fig. 10a) lags \tilde{u}' (Fig. 3a) by a quarter cycle because of the time-mean upper-level wind is easterly over the warm pool (Fig. 12c). $-\tilde{u}'\frac{\partial[\tilde{u}]}{\partial x}$ (Fig. 10b) is out of phase with \tilde{u}' because the time-mean upper level zonal divergence is positive over the warm pool (Fig. 12b). $-\tilde{u}'\frac{\partial\tilde{u}'}{\partial p}$ (Fig. 11a) is out of phase with the upper-level \tilde{u}' (Fig. 3a) because zonal wind shear $\frac{\partial\tilde{u}'}{\partial p}$ is in phase with upper-level \tilde{u}' and the time-mean vertical motion is upward (negative $[\tilde{\omega}]$, Fig. 12a).

Why, then, is the local tendency much smaller than the advective tendency? We can understand this using a simple scale analysis. The basic scales for the MJO and the time-mean flow over the warm pool are:

$$T \approx 40 \text{ days} \qquad \text{period}$$

$L \approx 4 \times 10^7 \text{ m}$	zonal wavelength
$[\tilde{u}] \approx 10 \text{ m/s}$	time-mean upper-level zonal wind
$\frac{\partial[\tilde{u}]}{\partial x} \approx 0.2 \text{ day}^{-1}$	time-mean upper-level zonal divergence

From these scales we can estimate the magnitude of the local tendency and the dominant linear zonal advection terms:

$$\begin{aligned}
\frac{\partial \tilde{u}'}{\partial t} &\approx 2\tilde{u}'/(0.5T) \approx \tilde{u}'/(10 \text{ days}) \\
-[\tilde{u}] \frac{\partial \tilde{u}'}{\partial x} &\approx [\tilde{u}] \times 2\tilde{u}'/(0.5L) \approx \tilde{u}'/(10 \text{ days}) \\
-\tilde{u}' \frac{\partial [\tilde{u}]}{\partial x} &\approx \tilde{u}'/(5 \text{ days})
\end{aligned}$$

Therefore, the linear zonal advection terms is larger than the local tendency. Because the vertical advection terms enhance the zonal advection terms, the total advective tendency (Fig. 5c), when scaled using \tilde{u}' (Fig. 3a), is equivalent to a time-scale of 2-3 days, which is much shorter than the 10 days time-scale of local tendency. Therefore, the dominant balance between advective tendency and pressure gradient force is a physically robust feature for the MJO. This only holds at the MJO time-scale but not at shorter time-scales, and only in the warm pool region where time-mean zonal wind and zonal divergence are very large.

In summary, over the warm pool region, the strong climatological deep convection is associated with strong upward motion, strong upper-level zonal divergence, and strong upper-level easterly wind. Simple scale analysis shows that the magnitudes of these time-mean flows are bound to cause an advective tendency much larger than the local tendency at the MJO time-scale, leading to the dominant balance between

advective tendency and pressure gradient force.

5. Conclusions and discussions

This study examined the equatorial wave structure and zonal momentum budget of the MJO. The results are schematically shown in Fig. 14. The equatorial wave structure of the MJO is associated with a vertical mode concentrated in the upper half of the troposphere, with middle-troposphere inflow and near-tropopause outflow at the time of maximum precipitation. The vertical motion has a westward phase tilt with height. Geopotential height lags zonal wind by about 5-10 days at both the inflow and outflow layers.

A surprising finding is that the dominant balance of the MJO zonal momentum budget at the equator is between advective tendency and pressure gradient force. The local tendency is small, as well as the convective momentum flux convergence suggested by budget residual. The advective tendency is dominated by the linear terms associated with time-mean zonal and vertical motions. The warm pool region has the strongest climatological deep convection in the world. The deep convection is associated with strong upward motion ($[\omega] < 0$), strong upper-level zonal divergence ($\partial[u]/\partial x > 0$), and strong upper-level easterly wind ($[u] < 0$). When the MJO travels in such a large-scale environment, at the upper levels, $-[u]\partial u'/\partial x$ lags u' by a quarter cycle, while both $-u'\partial[u]/\partial x$ and $-[\omega]\partial u'/\partial p$ are out of phase with u' . Simple scale analysis shows that the magnitudes of the time-mean flows are bound to cause an advective tendency much larger than the local tendency at the MJO

time-scale, leading to the dominant balance between advective tendency and pressure gradient force. The simplified MJO zonal momentum equation is Eq. 8. Therefore, the observed MJO is dynamically different from the Kelvin wave, and the linear advection terms associated with time-mean flow need to be included when modeling the MJO wave structure.

Our results are in line with the finding of Slingo et al. (1996) that GCMs which produce more realistic intraseasonal variability also tend to produce a stronger seasonal cycle of basic flow. It would be interesting to study theoretically the effect of advection terms on the amplitude and phase speed of eastward-propagating intraseasonal modes. Here we present a very simple example by adding an advection term to the classic shallow-water Kelvin-wave model of Matsuno (1966), and look at its effect on the phase speed of the eastward-propagating mode. The model equations are:

$$\frac{\partial u'}{\partial t} = -\frac{\partial \phi'}{\partial x} - [u] \frac{\partial u'}{\partial x} \quad (9)$$

$$\frac{\partial \phi'}{\partial t} = -gh_e \frac{\partial u'}{\partial x} \quad (10)$$

The x and t dependences may be separated by specifying solutions in the form of zonally propagating waves: $u' = \hat{u} \exp[i(kx - \nu t)]$, $\phi' = \hat{\phi} \exp[i(kx - \nu t)]$.

$$-i\nu \hat{u} = ik\hat{\phi} - ik[u]\hat{u} \quad (11)$$

$$-i\nu \hat{\phi} = -gh_e(ik\hat{u}) \quad (12)$$

If Eq. 11 is solved for \hat{u} and the result substituted into Eq. 12 we obtain

$$(\nu/k)^2 - [u](\nu/k) - gh_e = 0$$

and the dispersion relation is

$$c \equiv \nu/k = ([u]/2) \pm \sqrt{([u]/2)^2 + gh_e} \quad (13)$$

We only look at the solution with plus sign because $[u] < 0$ over the warm pool and we are interested in eastward-propagating waves ($c > 0$). The variation of phase speed with equivalent depth h_e and time-mean zonal wind $[u]$ is shown in Fig. 15a and its difference with the no advection ($[u] = 0$) case is shown in Fig. 15b. The observed equivalent depth in the tropical atmosphere is between 12 to 50 m (Wheeler and Kiladis 1999), and the seasonal mean 150 mb zonal wind over the warm pool is between -3 m/s to -20 m/s (Fig. 13c). Fig. 15b shows that over this range of parameters, adding the advection term can reduce the phase speed by 3-7 m/s. Therefore, advection associated with mean zonal wind reduces the phase speed substantially. In this very simple model the diabatic heating is not explicitly treated, although it is reflected in the reduced equivalent depth (Wheeler and Kiladis 1999). It would be much more interesting to use models with convection parameterizations to study the influence of advection terms on the different wave-convection feedback mechanisms, and on the instability and phase speed of the intraseasonal modes.

Appendix. Decomposition of the advection terms

Because the MJO anomaly in this study does not include the zonal mean, decomposition of the advection terms is more complex than when zonal mean is retained.

Following Peixoto and Oort (1992, pp61-64), a quantity A can be decomposed into:

$$A = [\overline{A}] + [\tilde{A}] + \overline{A'} + \tilde{A'} \quad (\text{A1})$$

where overbar represents zonal mean, tilde represents deviation from the zonal mean (zonal asymmetric component), bracket represents time mean, and prime represents deviation from the time mean. It can be derived that:

$$\begin{aligned} \widetilde{AB'} = ([\tilde{A}]\tilde{B'} + [\tilde{B}]\tilde{A'}) + ([\overline{A}]\tilde{B'} + [\overline{B}]\tilde{A'}) + ([\tilde{A}]\overline{B'} + [\tilde{B}]\overline{A'}) \\ + (-[\overline{\tilde{A}}]\overline{\tilde{B'}} - [\overline{\tilde{B}}]\overline{\tilde{A'}} + \widetilde{A'B'} - [\widetilde{A'B'}]) \end{aligned} \quad (\text{A2})$$

On the right hand of the equation, the terms on the first line are the linear terms, among which the first two are associated with time-mean zonal asymmetric component, and are calculated in Eqs. 6 and 7. The third and fourth are associated with time-mean zonal-mean component. The fifth and sixth are associated with temporally filtered zonal-mean component. The terms on the second line are the nonlinear terms. When considering only the 30-70 day anomalies, the nonlinear terms will include some more terms corresponding to interaction with other time-scales.

REFERENCES

- Bergman, J. W., H. H. Hendon, K. M. Weickmann, 2001: Intraseasonal Air-Sea Interactions at the Onset of El Nino. *Journal of Climate*, **14**, 1702-1719.
- Carr, Matthew T., Bretherton, Christopher S. 2001: Convective Momentum Transport over the Tropical Pacific: Budget Estimates. *J. Atmos. Sci.*, **58**, 1673-1693.
- Chang, C. P., 1977: Viscous internal gravity waves and low-frequency oscillations in the tropics. *J. Atmos. Sci.*, **34**, 901-910.
- Chang, C. P., and H. Lim, 1988: Kelvin wave-CISK: A possible mechanism for the 30-50 day oscillations. *J. Atmos. Sci.*, **45**, 1709-1720.
- Cho, H.-R., K. Fraedrich, and J. T. Wang, 1994: Cloud clusters, Kelvin wave-CISK , and the Madden-Julian oscillations in the equatorial troposphere. *J. Atmos. Sci.*, **51**, 68-76.
- Crum, F. R., and T. J. Dunkerton, 1992: Analytic and numerical models of wave-CISK with conditional heating. *J. Atmos. Sci.*, **49**, 1693-1708.
- Duchan, C.E., 1979: Lanczos filtering in one and two dimensions. *J. Appl. Meteor.*, **18**, 1016-1022.
- Emanuel, K. A., 1987: An air-sea interaction model of intraseasonal oscillation in the Tropics. *J. Atmos. Sci.*, **44**, 2324-2340.
- Gallus, William A., Johnson, Richard H. 1992: The Momentum Budget of an Intense Midlatitude Squall Line. *J. Atmos. Sci.*, **49**, 422-450.
- Gill, A. E., 1980: Some simple solutions for heat-induced tropical circulation. *Quart. J. Roy. Meteor. Soc.*, **106**, 447-462.

- Hayashi, Y., and A. Sumi, 1986: The 30-40 day oscillation simulated in an "aqua planet" model. *J. Meteor. Soc. Japan.*, **64**, 451-466.
- Hayashi, Y., and D. G. Golder, 1986: Tropical intraseasonal oscillations appearing in a GFDL general circulation model and FGGE data. Part I: Phase propagation. *J. Atmos. Sci.*, **43**, 3058-3067.
- Hayashi, Y., and D. G. Golder, 1988: Tropical intraseasonal oscillations appearing in a GFDL general circulation model and FGGE data. Part II: Structure. *J. Atmos. Sci.*, **45**, 3017-3033.
- Hayashi, Y., and D. G. Golder, 1993: Tropical 40-50 and 25-30-day oscillations appearing in realistic and idealized GFDL climate models and the ECMWF dataset. *J. Atmos. Sci.*, **50**, 464-494.
- Hendon, H. H., and B. Liebmann, 1990: A composite study of onset of the Australia monsoon. *J. Atmos. Sci.*, **47**, 2227-2240.
- Hsu, H.-H., 1996: Global view of the intraseasonal oscillation during northern winter. *J. Climate*, **9**, 2386-2406.
- Inness, P. M., and D. Gregory, 1997: Aspects of the intraseasonal oscillation simulated by the Hadley Centre Atmosphere Model. *Climate Dyn.*, **13**, 441-458.
- Kessler, W. S., and M. J. McPhaden, and K. M. Weickmann, 1995: Forcing of intraseasonal Kelvin waves in the equatorial Pacific. *J. Geophys. Res.*, **100**, 10613-10631.
- Kiladis, G. N., and K. M. Weickmann, 1992: Circulation anomalies associated with tropical convection during northern winter. *Mon. Wea. Rev.*, **120**, 1900-1923.
- Knutson, T. R., and K. M. Weickmann, 1987: 30-60 day atmospheric oscillations: Com-

- posite life cycles of convection and circulation anomalies. *Mon. Wea. Rev.*, **115**, 1407-1436.
- Lau, K. M., and P. H. Chan, 1985: Aspects of the 40-50-day oscillation during the northern winter as inferred from outgoing longwave radiation. *Mon. Wea. Rev.*, **113**, 1889-1909.
- Lau, K. M., and L. Peng, 1987: Origin of low-frequency (intraseasonal) oscillations in the tropical atmosphere. *J. Atmos. Sci.*, **44**, 950-972.
- Lau, K.-M., and T. J. Phillips, 1986: Coherent fluctuations of extratropical geopotential height and tropical convection in intraseasonal timescales. *J. Atmos. Sci.*, **43**, 1164-1181.
- Lau, N. C., I. M. Held, and J. D. Neelin, 1988: The Madden-Julian oscillations in an idealized general circulation model. *J. Atmos. Sci.*, **45**, 3810-3831.
- Liebmann, B., H. H. Hendon, and J. D. Glick, 1994: The relationship between the tropical cyclones of the western Pacific and Indian Oceans and the Madden-Julian oscillation. *J. Meteor. Soc. Japan*, **72**, 401-411.
- Lin, J., B. E. Mapes, M. H. Zhang, and M. Newman, 2003: Stratiform precipitation, vertical heating profiles, and the Madden-Julian Oscillation. *J. Atmos. Sci.*, in press.
- Lin, J., and B. E. Mapes, 2003: Role of convective momentum transport in tropical large-scale circulations. *J. Atmos. Sci.*, to be submitted.
- Lindzen, R. D., 1967: Planetary waves on beta-planes. *Mon. Wea. Rev.*, **95**, 441-451.
- Madden, R. A., and P. R. Julian, 1971: Detection of a 40-50 day oscillation in the zonal wind in the tropical Pacific. *J. Atmos. Sci.*, **28**, 702-708.

- Madden, R. A., and P. R. Julian, 1972: Description of global-scale circulation cells in the tropics with a 40-50 day period. *J. Atmos. Sci.*, **29**, 1109-1123.
- Madden, R. A., and P. R. Julian, 1994: Observations of the 40-50-day oscillation -A review. *Mon. Wea. Rev.*, **122**, 814-837.
- Mapes, B. E., Wu, X. 2001: Convective Eddy Momentum Tendencies in Long Cloud-Resolving Model Simulations. *J. Atmos. Sci.*, **58**, 517-526.
- Matsuno, T., 1966: Quasi-geostrophic motions in the equatorial area. *J. Meteor. Soc. Japan*, **44**, 25-43.
- Mehta, A. V., and E. A. Smith, 1997: Variability of radiative cooling during the Asian summer monsoon and its influence on intraseasonal waves. *J. Atmos. Sci.*, **54**, 941-966.
- Murakami, M., 1979: Large-scale aspects of deep convective activity over the GATE area. *Mon. Wea. Rev.*, **107**, 994-1013.
- Nakazawa, T., 1986: Mean features of 30-60 day variations as inferred from 8-year OLR data. *J. Meteor. Soc. Japan*, **64**, 777-786.
- Neelin, J. D., I. M. Held, and K. H. Cook, 1987: Evaporation-wind feedback and low-frequency variability in the tropical atmosphere. *J. Atmos. Sci.*, **44**, 2341-2348.
- Oort, A. H., and J. J. Yienger, 1996: Observed long-term variability in the Hadley circulation and its connection to ENSO. *J. Climate*, **9**, 2751-2767.
- Salby, M. L., and H. H. Hendon, 1994: Intraseasonal behavior of clouds, temperature, and motion in the Tropics. *J. Atmos. Sci.*, **51**, 2207-2224.
- Slingo, J. M., and Coauthors, 1996: Intraseasonal oscillations in 15 atmospheric general

- circulation models: Results from an AMIP diagnostic subproject. *Climate Dyn.*, **12**, 325-357.
- Stevens, D. E., 1979: Vorticity, momentum, and divergence budgets of synoptic-scale wave disturbances in the tropical eastern Atlantic. *Mon. Wea. Rev.*, **107**, 535-550.
- Takayabu, Y .N., Toshio Iguchi, Misako Kachi, Akira Shibata and Hiroshi Kanzawa, 1999: Abrupt termination of the 1997-98 El Nino in response to a Madden-Julian oscillation. *Nature*, 402, 279-282.
- Wang, B., 1988: Dynamics of tropical low-frequency waves: An analysis of the moist Kelvin wave. *J. Atmos. Sci.*, **45**, 2051-2065.
- Wang, B., and H. Rui, 1990: Synoptic climatology of transient tropical intraseasonal convection anomalies. *Meteor. Atmos. Phys.*, **44**, 43-61.
- Weickmann, K. M., G. R. Lussky, and J. E. Kutzbach, 1985: Intraseasonal (30-60 day) fluctuations of outgoing longwave radiation and 250 mb streamfunction during northern winter. *Mon. Wea. Rev.*, 113, 941-961.
- Wheeler, M., and G. N. Kiladis, 1999: Convectively coupled equatorial waves: Analysis of clouds and temperature in the wavenumber-frequency domain. *J. Atmos. Sci.*, **56**, 374-399.
- Wu, X., and M. Yanai, 1994: Effect of vertical wind shear on the cumulus transport of momentum: Observations and parameterization. *J. Atmos. Sci.*, **51**, 1640-1660.
- Xie, P., and P. A. Arkin, 1997: Global precipitation: A 17-year monthly analysis based on gauge observations, satellite estimates, and numerical model outputs. *Bull. Amer. Meteor. Soc.*, **78**, 2539-2558.

- Yasunari, T., 1979: Cloudiness fluctuations associated with the northern hemisphere summer monsoon. *J. Meteor. Soc. Japan*, 57, 227-242.
- Zhang, M. H., and J. L. Lin, 1997: Constrained variational analysis of sounding data based on column-integrated budgets of mass, heat, moisture, and momentum: Approach and application to ARM measurements. *J. Atmos. Sci.*, **54**, 1503-1524.

FIGURE CAPTIONS

Fig. 1 Schematic depiction of the convectively coupled Kelvin wave. Regions of enhanced large-scale convection are indicated schematically by the clouds. The dark shading inside the clouds represents the maximum of the diabatic heating. “H” and “L” represent the high and low geopotential height anomalies, respectively. Thin arrows represent the anomalous wind. Thick arrows represent components of zonal momentum budget.

Fig. 2 The response function of the Murakami filter used in this study.

Fig. 3 The vertical structure of the MJO anomaly for (a) zonal wind (m/s), (b) vertical velocity (mb/day), and (c) geopotential height (m) for the 15 years (1979-1993) of NCEP reanalysis data averaged over 150E-160E and 5N-5S. Negative values are shaded. The arrows in (c) are the wind vectors whose horizontal component is the zonal wind, and vertical component the vertical velocity.

Fig. 4 Same as Fig. 3 except for data averaged over 80E-90E and 5N-5S.

Fig. 5 Terms of the MJO zonal momentum budget: (a) local tendency $\frac{\partial \tilde{u}'}{\partial t}$, (b) pressure gradient force $-\frac{\partial \tilde{\phi}'}{\partial x}$, and (c) advection terms $(-\widetilde{u \frac{\partial u}{\partial x}}' - \widetilde{v \frac{\partial u}{\partial y}}' - \widetilde{\omega \frac{\partial u}{\partial p}}')$, for 15 years (1979-1993) of NCEP reanalysis data averaged over 150E-160E and 5N-5S. Unit is $ms^{-1}day^{-1}$.

Fig. 6 As in Fig. 5 except for ECMWF reanalysis data.

Fig. 7 As in Fig. 5 except for the residual term \tilde{X}' for (a) NCEP reanalysis, and (b) ECMWF reanalysis.

Fig. 8 As in Fig. 5 except for the implied eddy momentum flux for (a) NCEP reanalysis, and (b) ECMWF reanalysis. Unit is N/m^2 .

Fig. 9 As in Fig. 5 except for three advection terms for NCEP reanalysis data: (a) zonal advection $-\widetilde{u \frac{\partial u}{\partial x}}'$, (b) meridional advection $-\widetilde{v \frac{\partial u}{\partial y}}'$, and (c) vertical advection $-\widetilde{\omega \frac{\partial u}{\partial p}}'$.

Fig. 10 As in Fig. 5 except for three components of the zonal advection term for NCEP reanalysis data: (a) $-\widetilde{[u] \frac{\partial u'}{\partial x}}$, (b) $-\widetilde{u' \frac{\partial [u]}{\partial x}}$, and (c) other terms.

Fig. 11 As in Fig. 5 except for three components of the vertical advection term for NCEP reanalysis data: (a) $-\widetilde{[\omega] \frac{\partial u'}{\partial p}}$, (b) $-\widetilde{\omega' \frac{\partial [u]}{\partial p}}$, and (c) other terms.

Fig. 12 Annual mean (a) $[\widetilde{\omega}]$ (mb/day), (b) $\frac{\partial [\widetilde{u}]}{\partial x}$ (1/day), and (c) $[\widetilde{u}]$ (m/s), for 15 years (1979-1993) of NCEP reanalysis data along the equator (5N-5S).

Fig. 13 Seasonal variation of (a) $[\widetilde{\omega}]$ (mb/day) at 300 mb, (b) $\frac{\partial [\widetilde{u}]}{\partial x}$ (1/day) at 150 mb, and (c) $[\widetilde{u}]$ (m/s) at 150 mb, for NCEP reanalysis data along the equator (5N-5S).

Fig. 14 Schematic depiction of the time-mean flow over the warm-pool, and the observed MJO wave structure and zonal momentum budget. Regions of enhanced large-scale convection are indicated schematically by the clouds. The dark shading inside the clouds represents the maximum of the diabatic heating. “H” and “L” represent the high and low geopotential height anomalies, respectively. Thin arrows represent the winds. Thick arrows represent components of zonal momentum budget.

Fig. 15 (a) Variation of phase speed with equivalent depth h_e and time-mean zonal wind $[u]$. (b) Difference of the phase speed with $[u] = 0$ case.

Kelvin wave in an atmosphere at rest

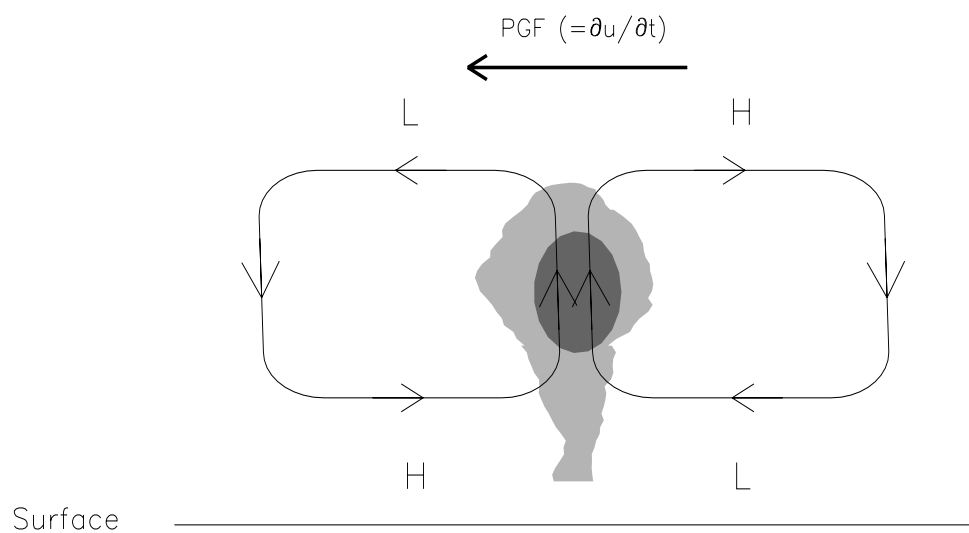


Figure 1:

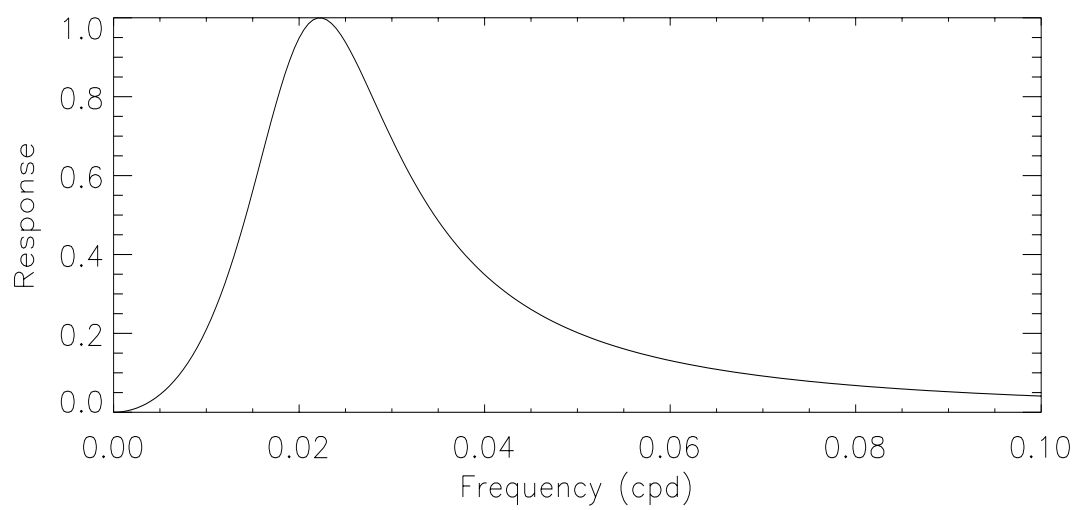


Figure 2:

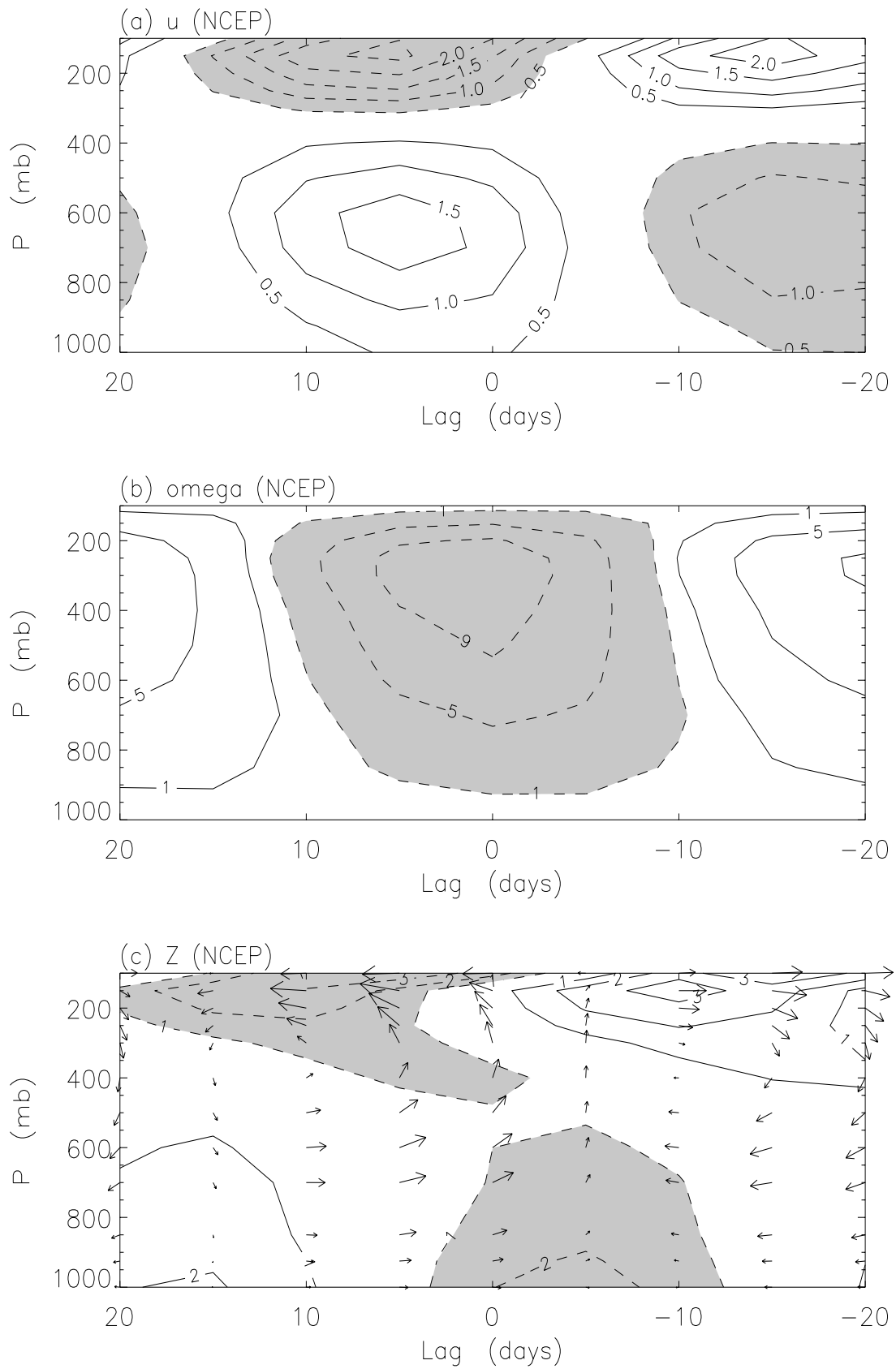


Figure 3:

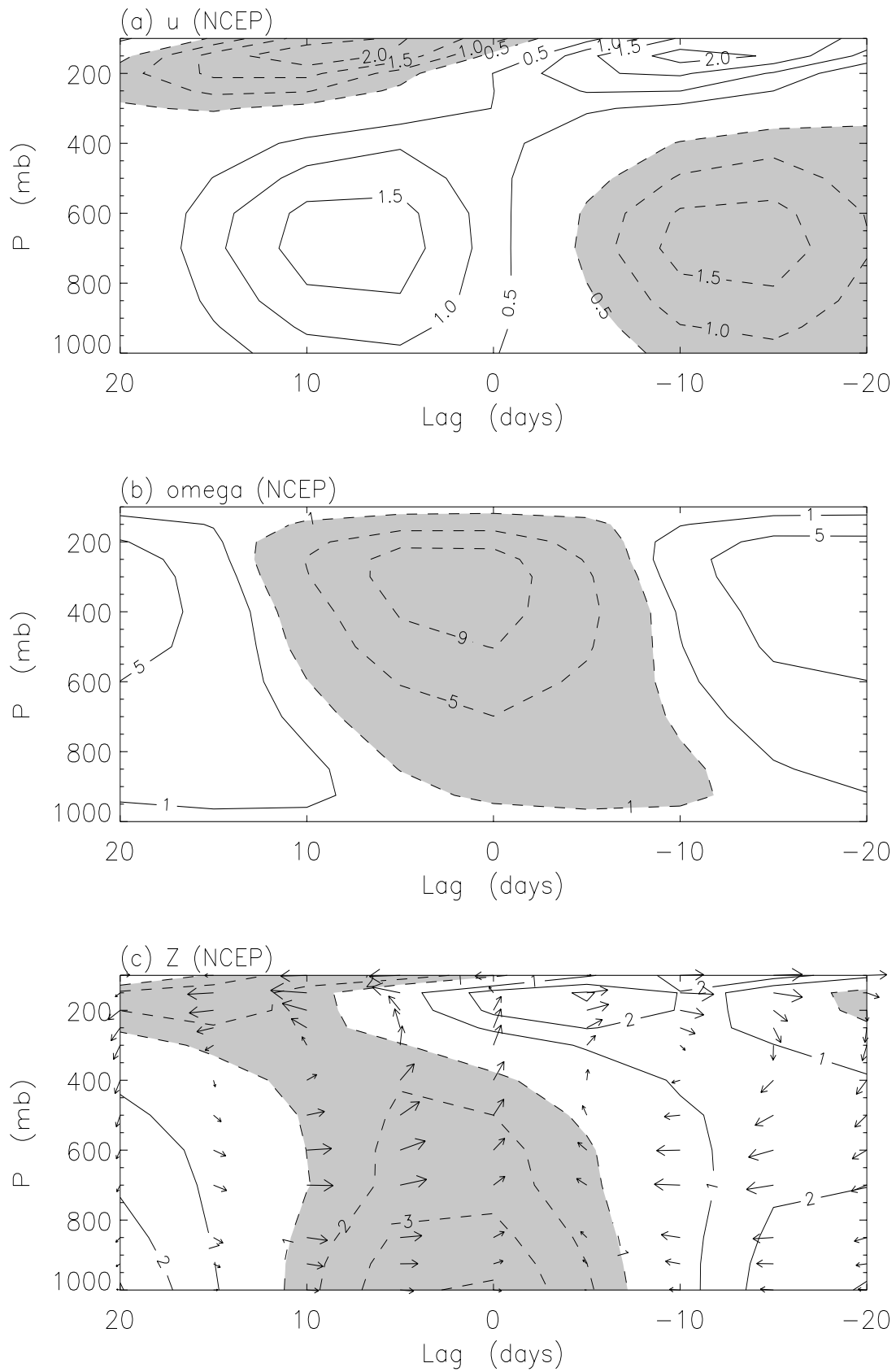


Figure 4:

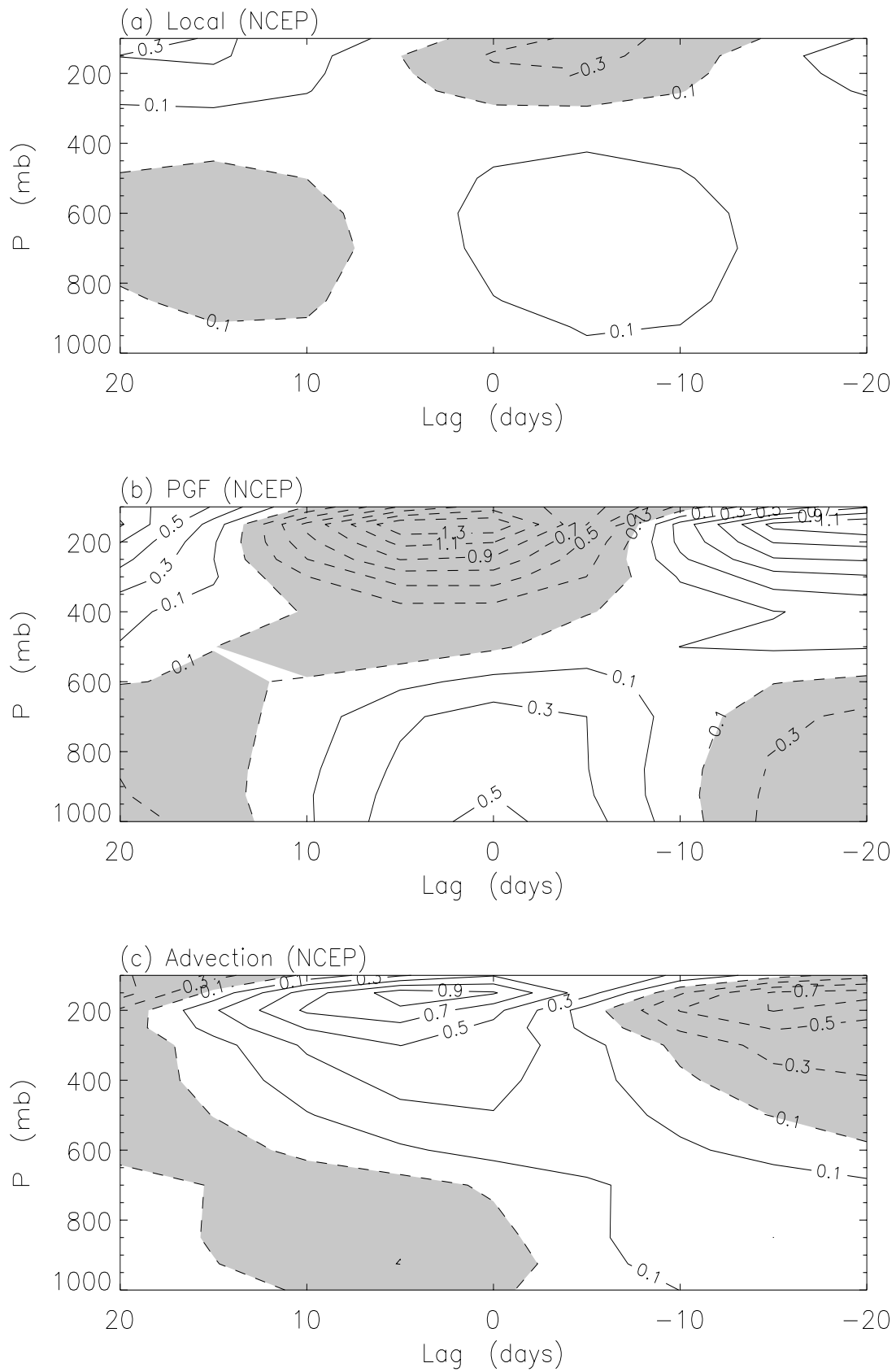


Figure 5:

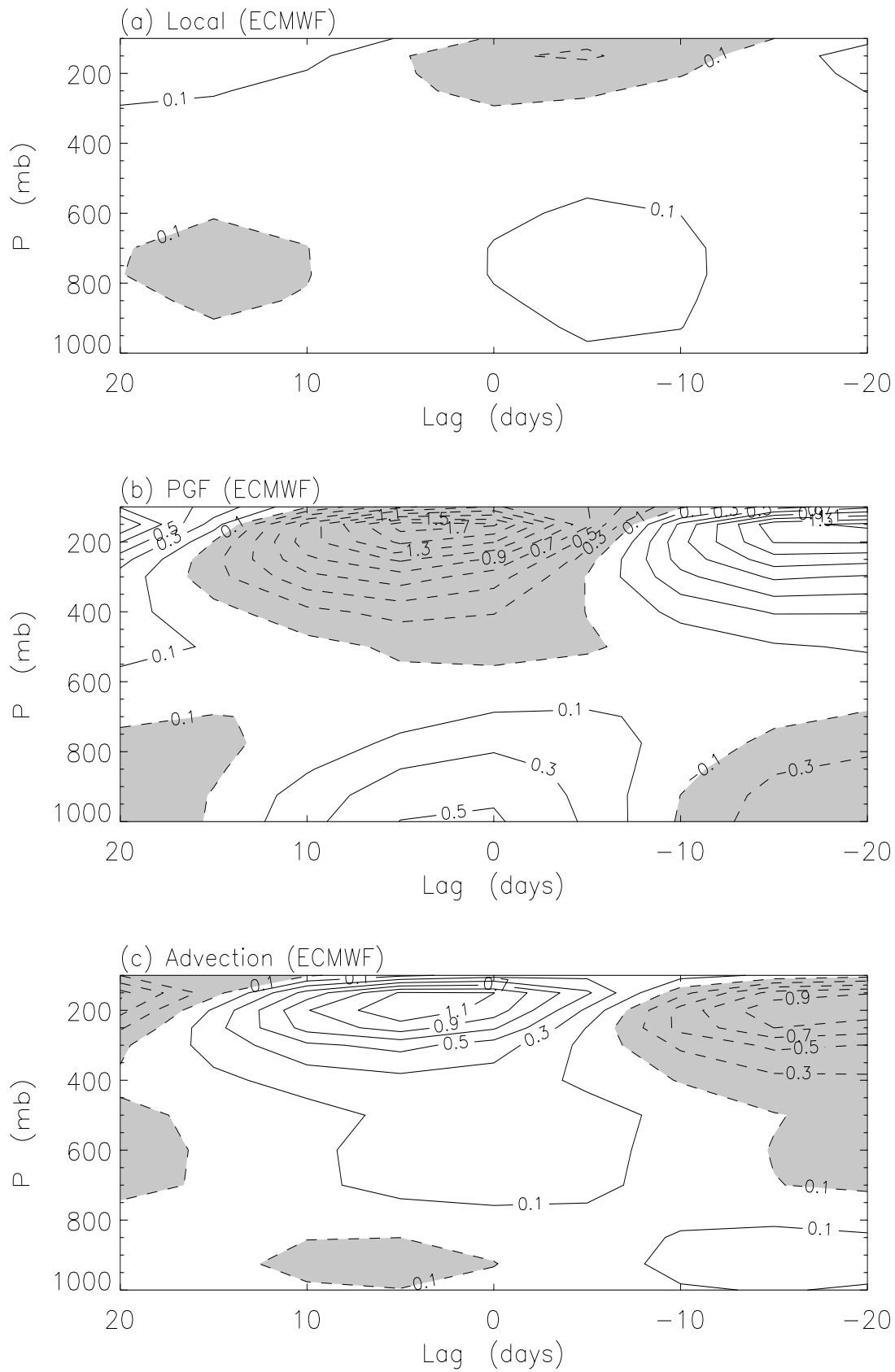


Figure 6:

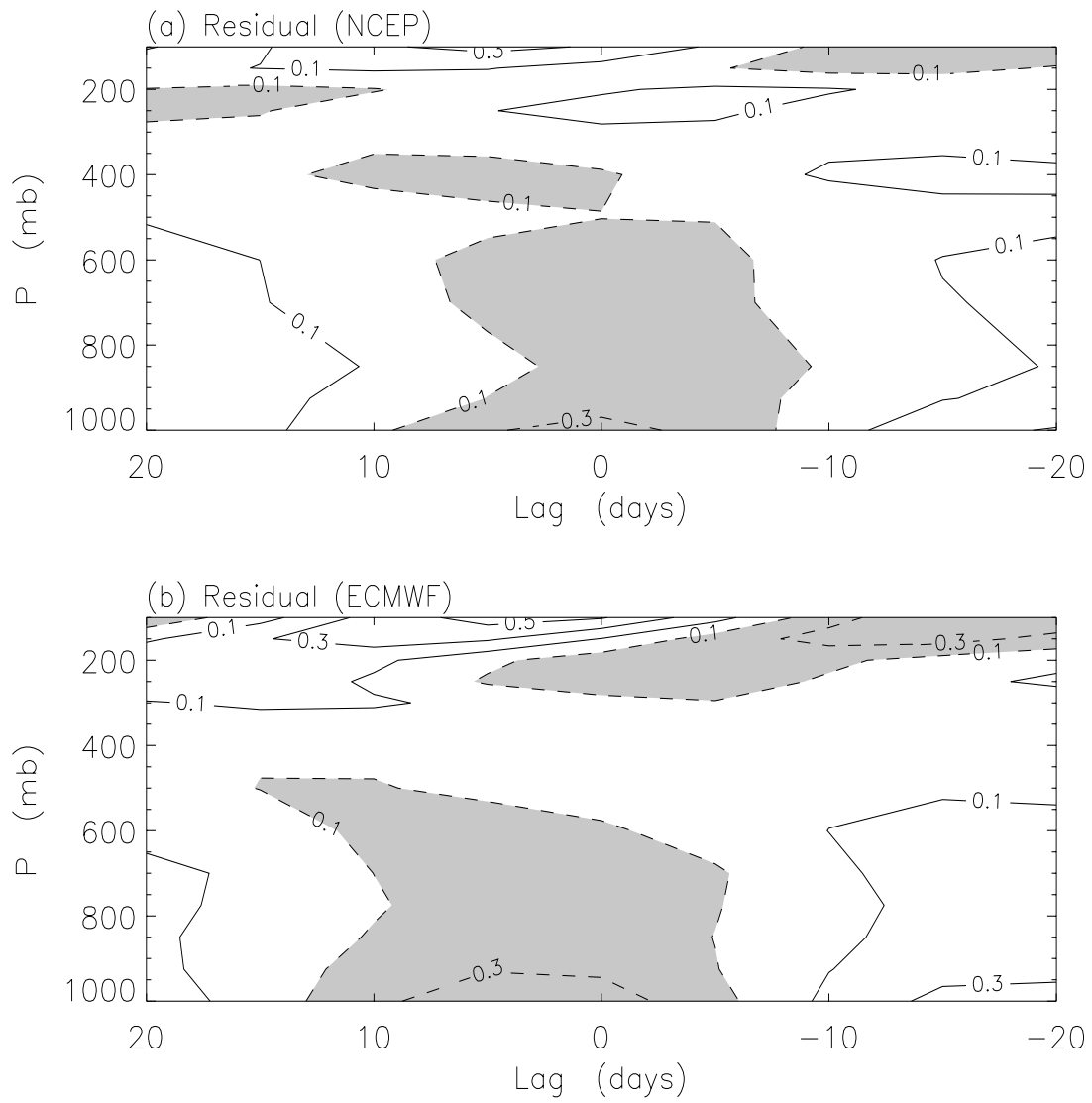


Figure 7:

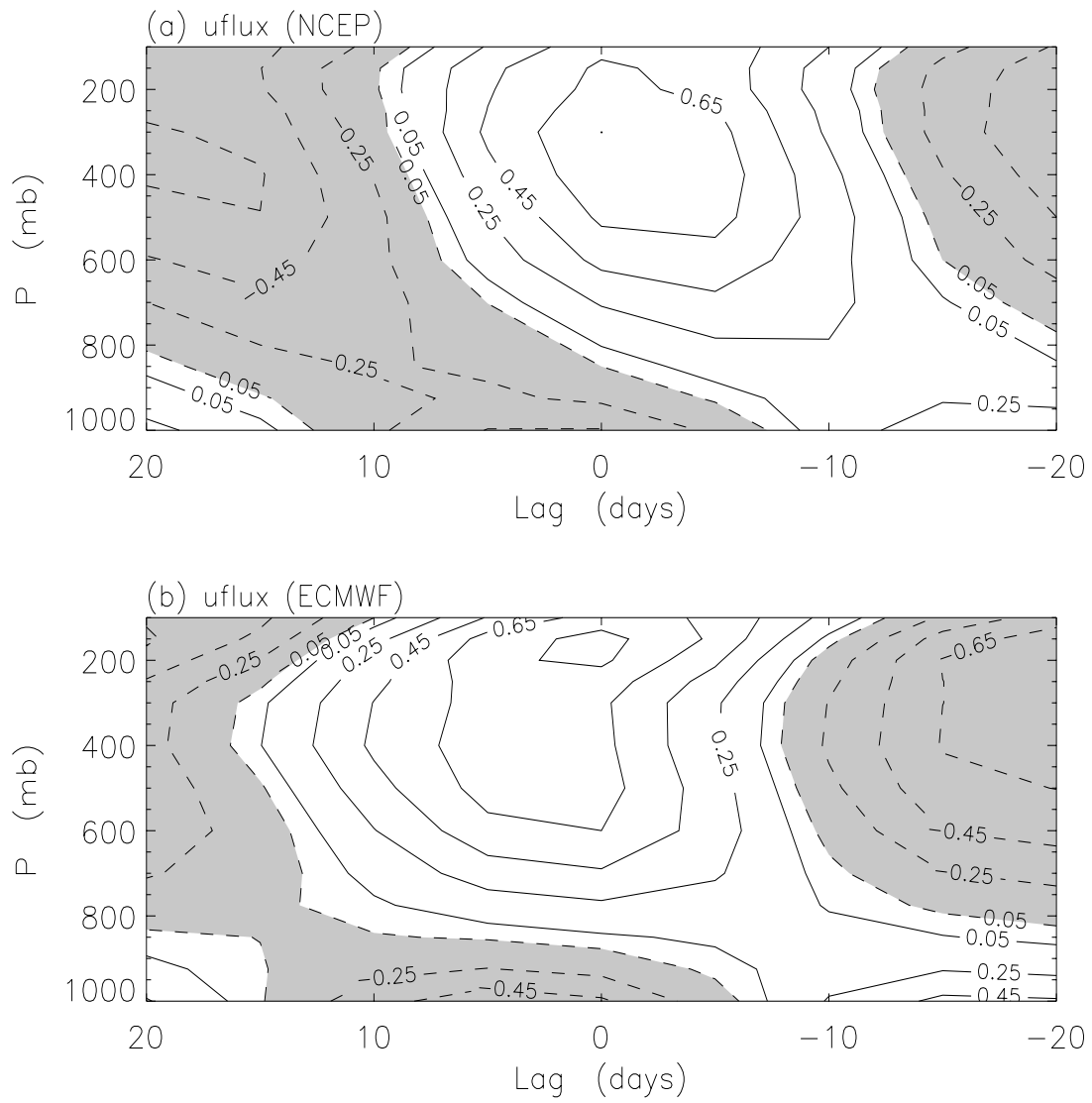


Figure 8:

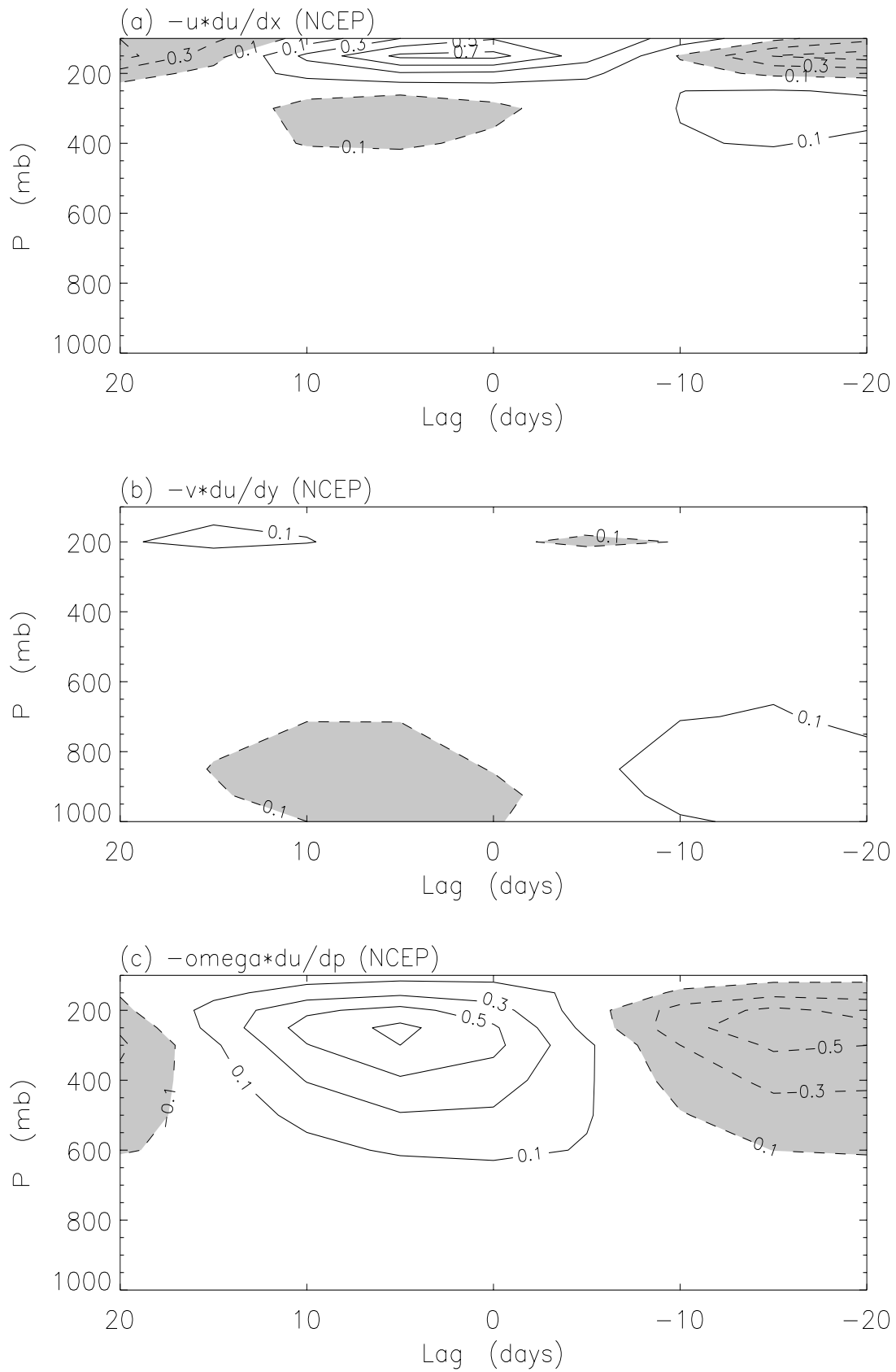


Figure 9:

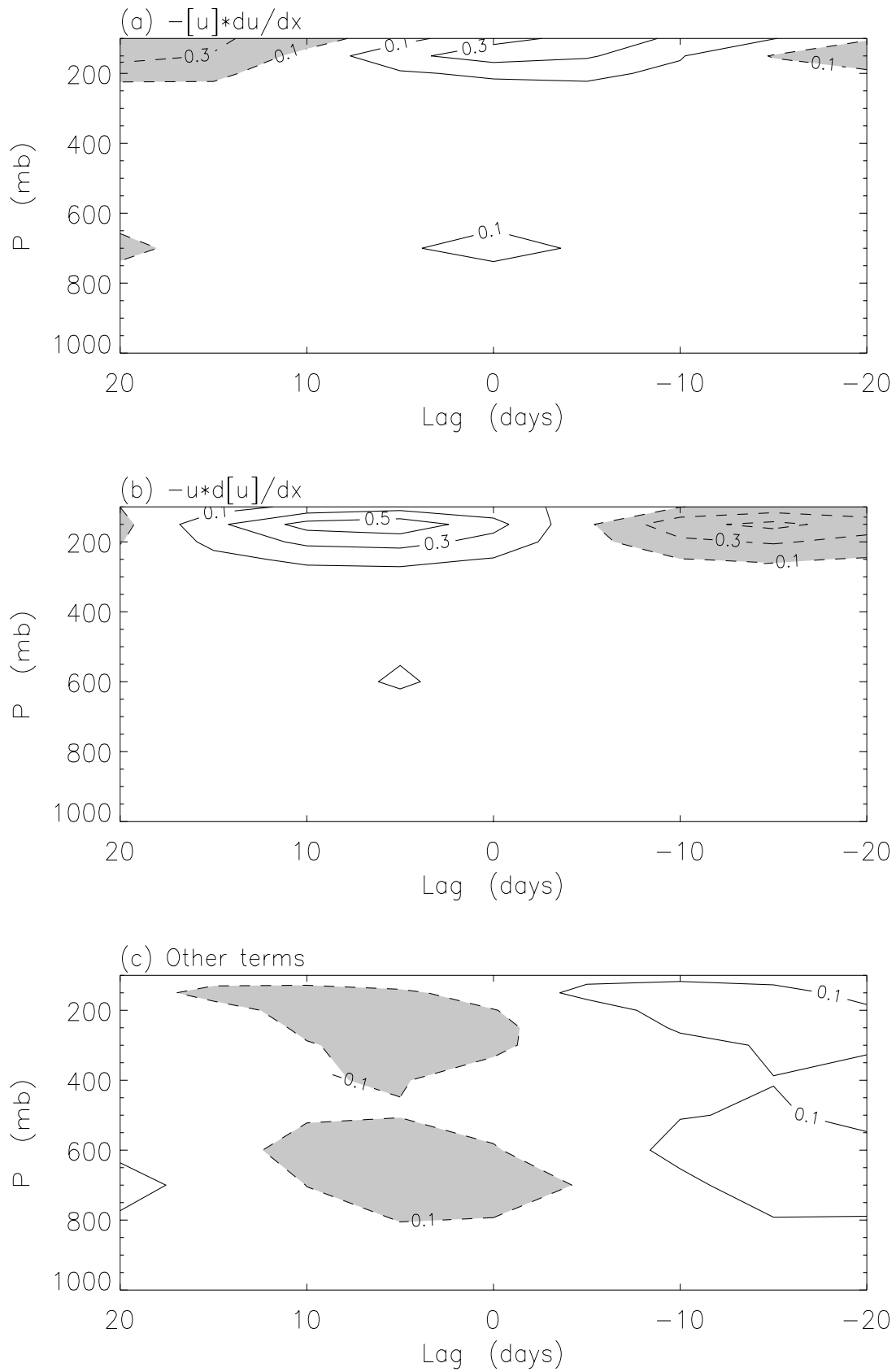


Figure 10:

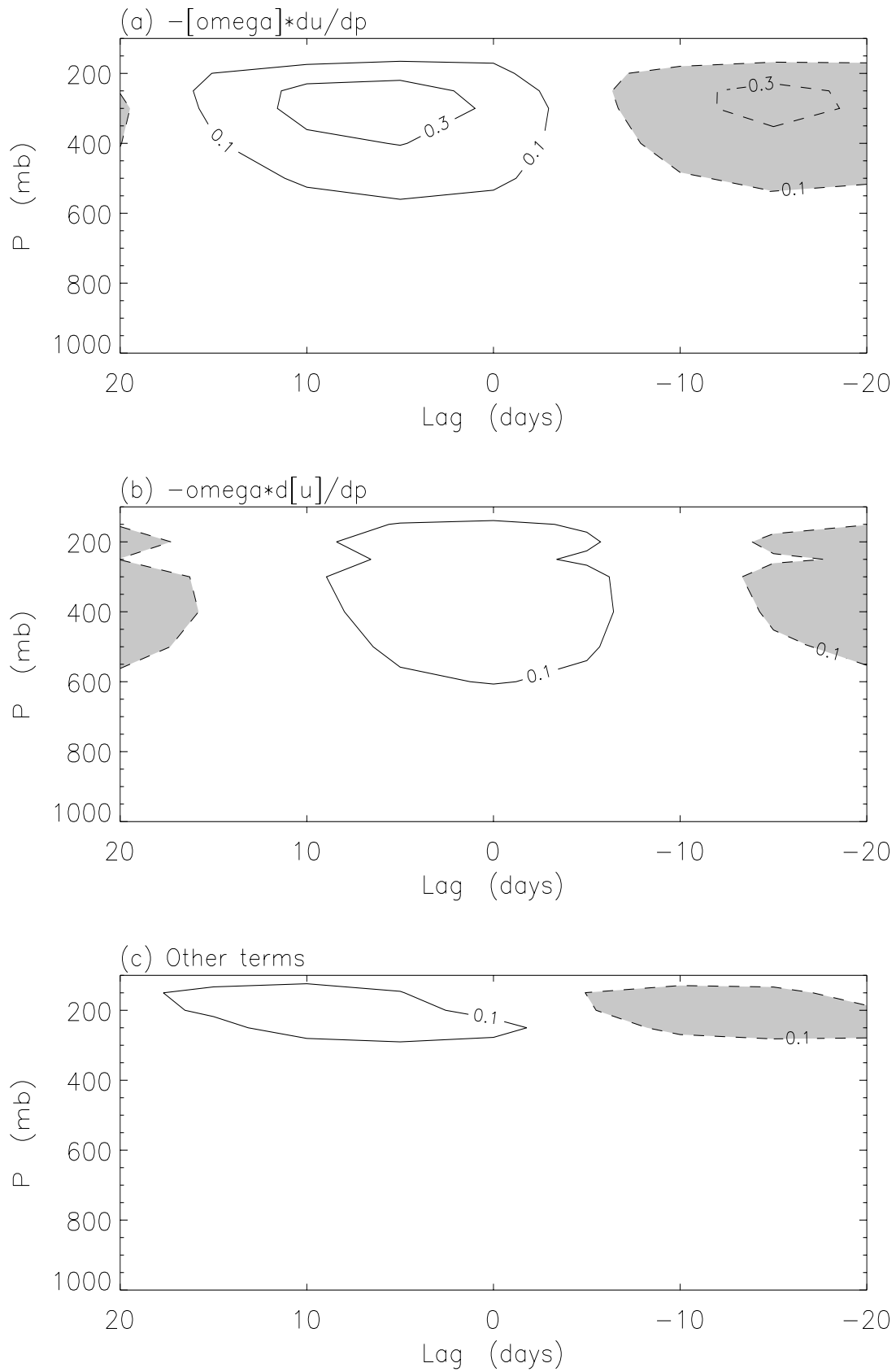


Figure 11:

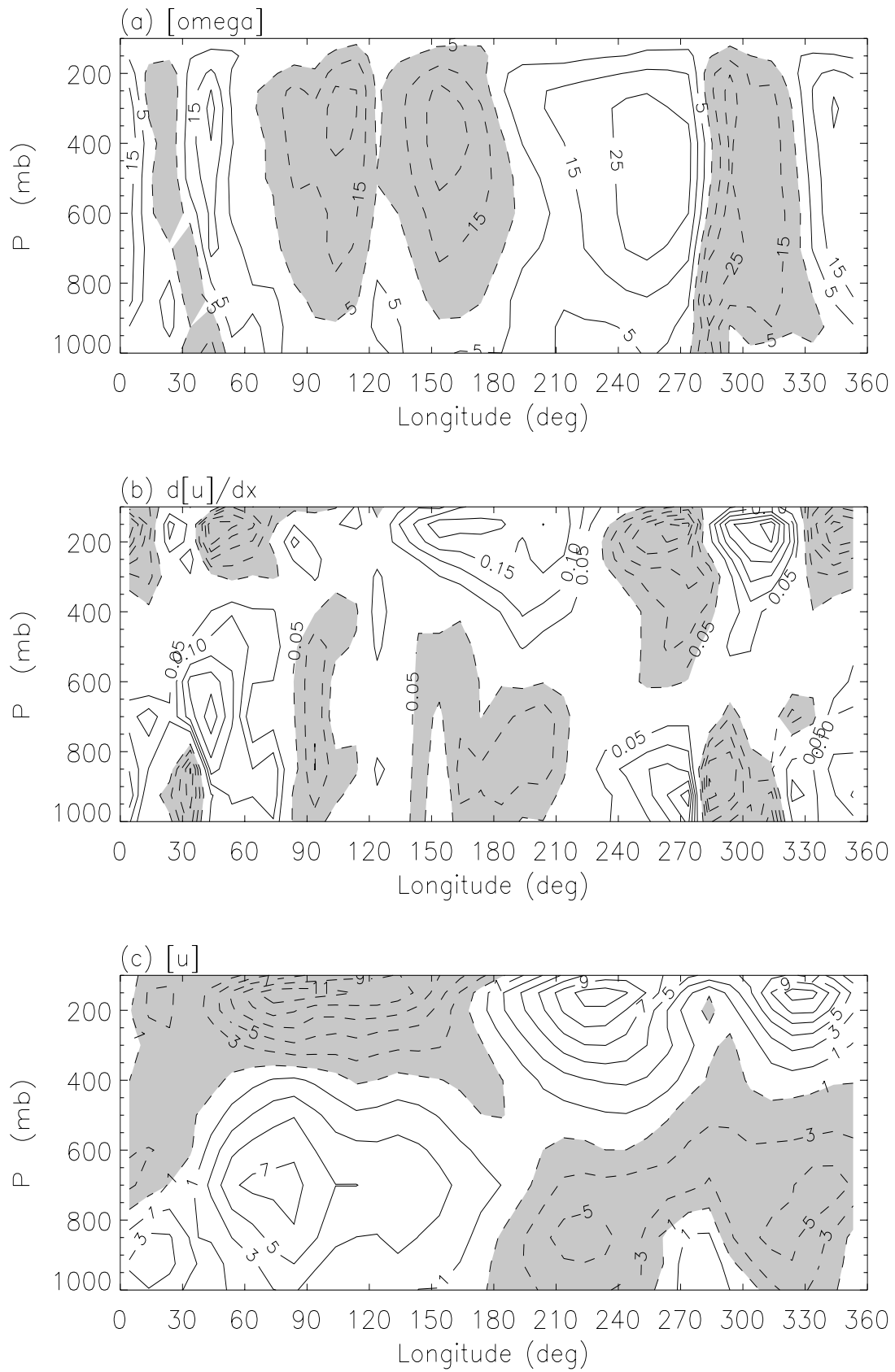


Figure 12:

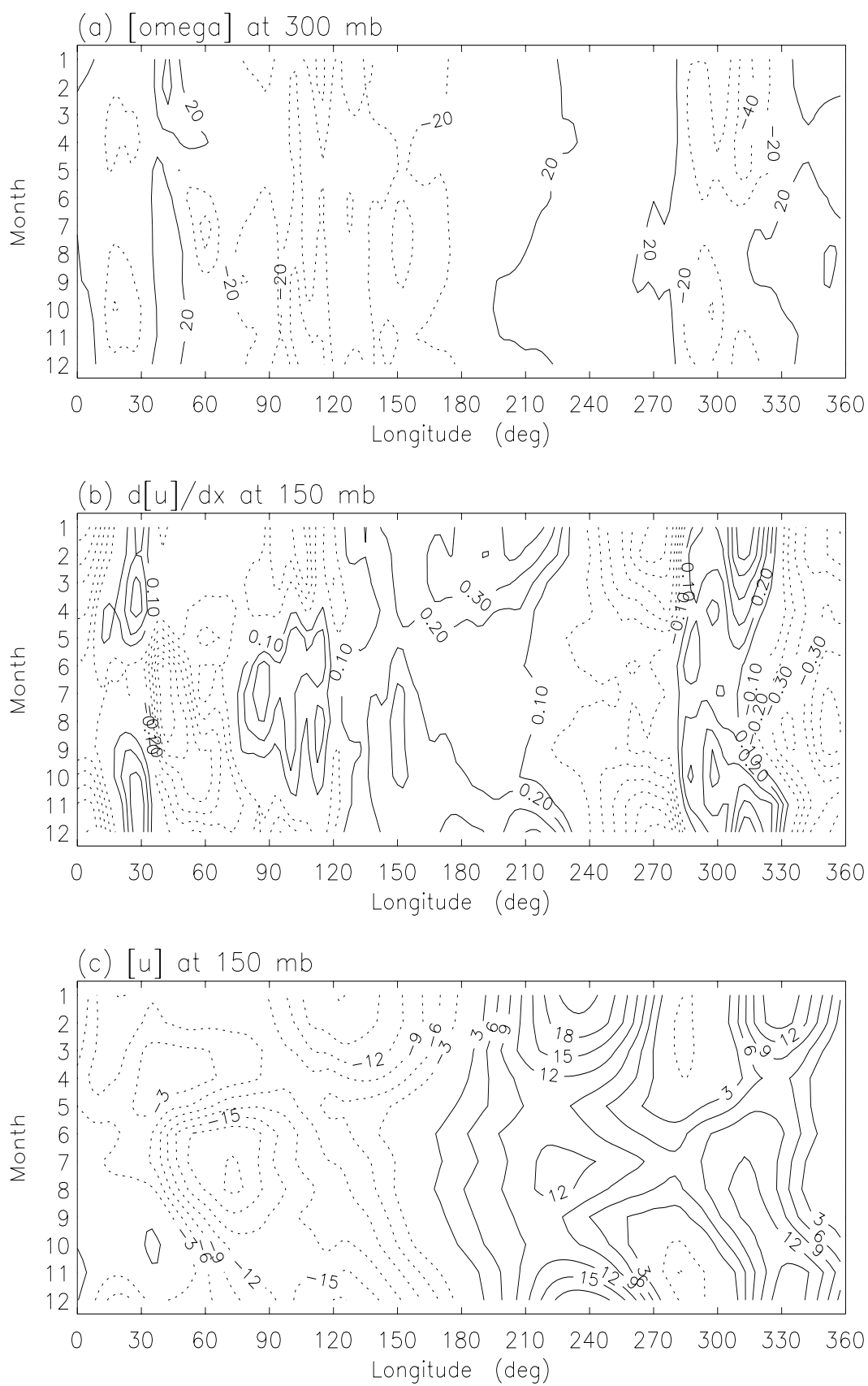


Figure 13:

MJO in warm-pool time-mean flow

Time-mean flow

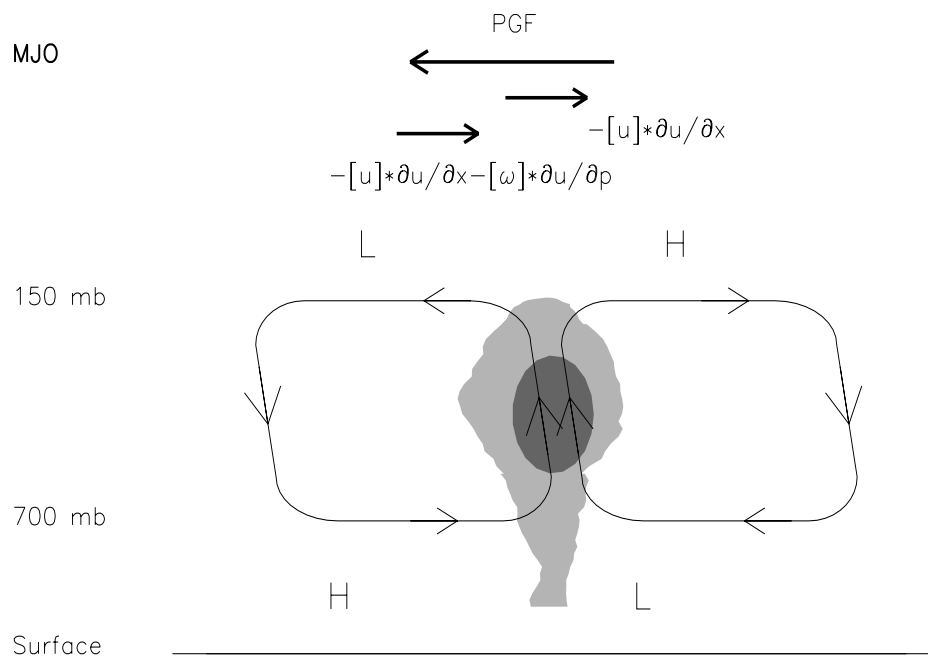
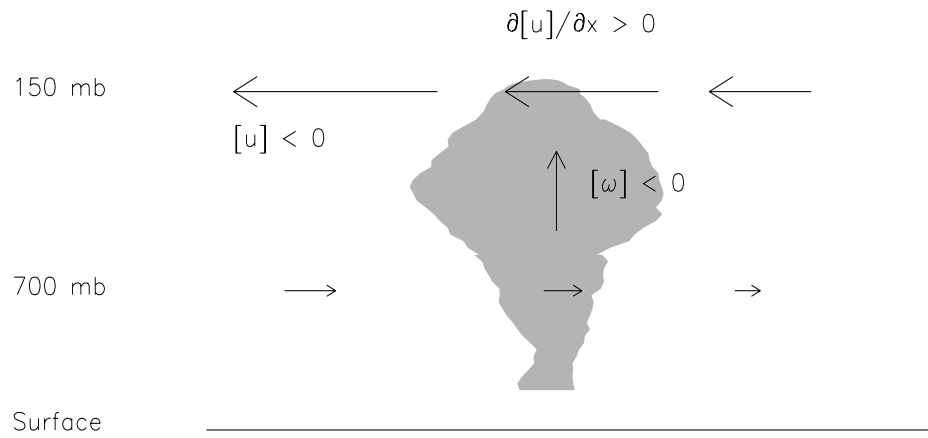


Figure 14:

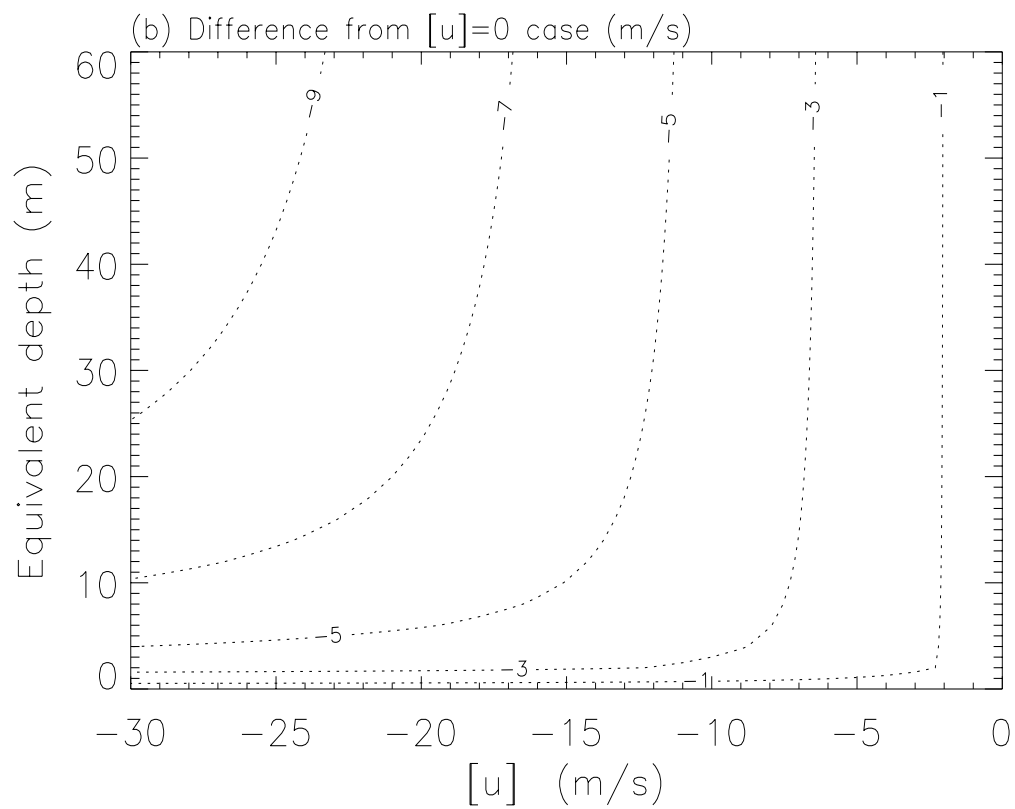
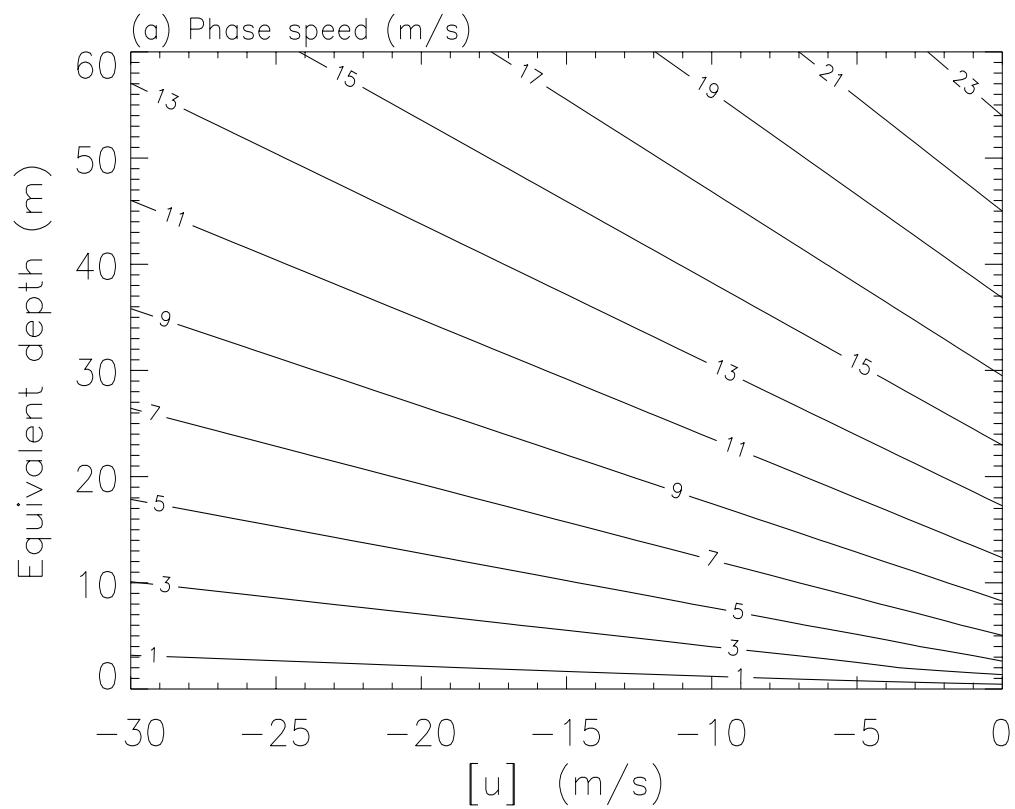


Figure 15: